Research Article | Vol. 27, No. 26 / 23 December 2019 / Optics Express 38147
Optics EXPRESS

Photon counting LIDAR at 2.3μm wavelength with superconducting nanowires

GREGOR G. TAYLOR,[1,*] DMITRY MOROZOV,[1] NATHAN R. GEMMELL,[2] KLEANTHIS EROTOKRITOU,[1] SHIGEHITO MIKI,[3,4] HIROTAKA TERAI,[4] AND ROBERT H. HADFIELD[1]

[1]James Watt School of Engineering, University of Glasgow, University Avenue, Glasgow G12 8QQ, UK
[2]University of Sussex, Falmer, Brighton BN1 9RH, UK
[3]Graduate School of Engineering Faculty of Engineering, Kobe University, 1-1 Rokkodai-cho, Nada, Kobe 657-0013, Japan
[4]Advanced ICT Research Institute, National Institute of Information and Communications Technology, 588-2 Iwaoka, Nishi-ku, Kobe, Hyogo 651-2492, Japan
[*]g.taylor.3@research.gla.ac.uk

Abstract: In this work, we show a proof-of-principle benchtop single-photon light detection and ranging (LIDAR) depth imager at 2.3μm, utilizing superconducting nanowire single-photon detectors (SNSPDs). We fabricate and fiber-couple SNSPDs to exhibit enhanced photon counting performance in the mid-infrared. We present characterization results using an optical parametric oscillator source and deploy these detectors in a scanning LIDAR setup at 2.3μm wavelength. This demonstrates the viability of these detectors for future free-space photon counting applications in the mid-infrared where atmospheric absorption and background solar flux are low.

1. Introduction

Photon counting light detection and ranging (LIDAR) is an accurate and fast optical measurement method for obtaining range information of targets [1]. Time-of-flight LIDAR is an elegant technique where a pulsed light source is used to deliver light pulses to the target. A start (sync) signal is measured when the pulse leaves the transceiver and a stop signal taken when returns from the target are recorded. In this way, by using elementary calculation, the distance of the reflected returns can be computed. The addition of a scanning transceiver or moveable target stage then makes high accuracy three dimensional depth images possible using this scheme [2]. The availability of high sensitivity detectors for these systems allows short integration times per pixel and the ability to pick targets out of the noise in photon sparse returns.

Detectors for single-photon counting applications have been an area of intense research in recent years. Conventional semiconductor technologies such as Si photomultiplier tubes (PMTs) [3] and Si single-photon avalanche photodiodes (SPADs) [4] offer good efficiency and detection characteristics but their cut off wavelength is low and are not suitable for use in the near to mid-infrared. SiGe SPADs offer improved spectral range but this still does not yet extend beyond 1.55μm [5]. InGaAs SPADs extend this spectral range further to 1.7μm and provide good detection efficiencies while suffering from afterpulsing effects and large dark count rates [6,7]. Near IR InGaAs PMTs are also available for wavelengths up to 1.7μm but suffer from low detection efficiencies, less than 2% for commercially available units. For wavelengths in the 2 to 10 μm range both InAs and HgCdTe are small bandgap materials suitable for low energy photon detection [8,9] however the single-photon detection capability is still to be shown. A different approach to longer wavelengths is to frequency upconvert the mid-infrared photons to shorter

#380800 https://doi.org/10.1364/OE.27.038147
Journal © 2019 Received 21 Oct 2019; revised 3 Dec 2019; accepted 3 Dec 2019; published 16 Dec 2019

Optics EXPRESS

wavelengths, thereby allowing detection with, for example, an Si SPAD. Efficiencies have been demonstrated of up to 20% for schemes such as this [10].

Superconducting nanowire single-photon detectors (SNSPDs or SSPDs) [11] have established themselves in the last decade as the gold standard for infrared single-photon counting applications. They have demonstrated near unity system detection efficiency at 1.55μm [12], dark count rates as low as 10^{-3}counts per second [13], timing jitter of 3ps FWHM [14] and spectral sensitivity far into the mid-infrared [15–17]. Closed cycle cooling provides a practical alternative to liquid helium systems enabling SNSPDs to be deployed in a variety of applications in the field of quantum information processing [18–20], as well as a host of other uses in experiments as diverse as space to ground communication [21] and Raman fiber temperature sensing [19].

LIDAR imaging systems utilizing SNSPDs have been demonstrated at 1.55μm wavelength, achieving up to km ranges [22] and with mm scale resolution [23]. Demonstrations of sea fog monitoring with SNSPD based LIDAR schemes have been shown [24] and differential absorption gas sensing systems proposed [25].These systems leverage the low timing jitter to achieve excellent depth resolution for fast integration times and the high system efficiency to enable imaging with low signal returns. In this work we exploit the spectral sensitivity of the SNSPDs to extend our working wavelength above 2μm into the mid-infrared which takes advantage of lower solar irradiance and minimal atmospheric absorption.

2. Mid-infrared for free-space applications

For a wide variety of free-space optical applications, LIDAR among them, it is advantageous to move the working wavelength into the mid-infrared. For daylight operation the background solar irradiance will give a large contribution to the system background count rate. As the solar irradiance is approximately similar to a blackbody at 5778K we can see that this irradiance will tail off as the wavelength increases with the bulk of the power concentrated in the 400 to 750nm range. Figure 1 shows the solar irradiance up to 4μm wavelength. Another key consideration is

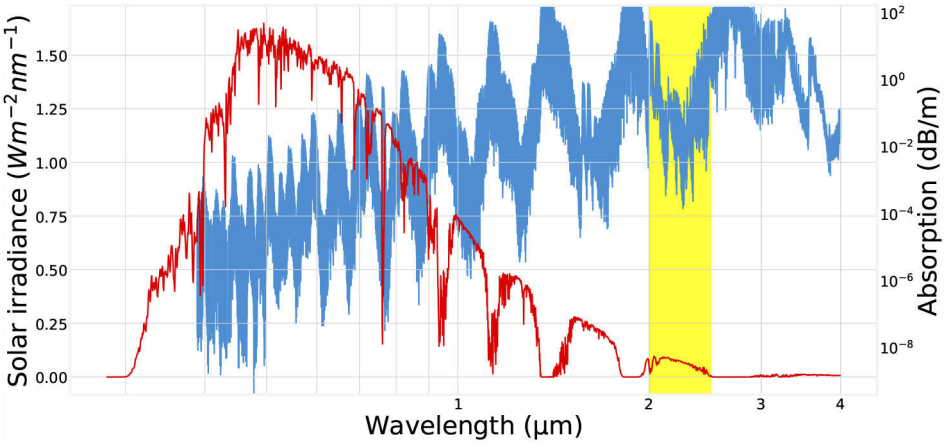

Fig. 1. Solar irradiance and atmospheric absorption. The red line shows the solar irradiance variation (left y-axis) with wavelength and the blue shows the combined absorption spectra of the most common molecules in the earth's atmosphere - H_2O, CO_2, O_2 and Ozone (right y-axis). The absorption is presented in dB per meter at 1 atmosphere and 296K temperature. The saturation at the top of the scale indicates 100% absorption for that wavelength. The solar data is from ASTM [26] and the spectral line data from HITRAN 2016 [27]. The highlighted region spans the 2 to 2.5μm range and shows a window of low absorption and lower background irradiance when compared to shorter wavelengths.

Optics EXPRESS

that atmospheric absorption has a strong wavelength dependence due to the variety of molecular absorption lines present in the atmosphere. The atmospheric absorption bands are also plotted in Fig. 1 for the most common atmospheric components. As we can see from the highlighted area, the range between 2 and 2.5μm offers a window of low solar irradiance, three times as low as at 1.55μm, and low atmospheric absorption which can be exploited for free-space applications. Similar windows exist at longer wavelengths, for example an additional low-absorption window can be seen in Fig. 1 just below 4μm which exhibits even lower solar background. However, blackbody radiation from room temperature optical components coupling into the detector begins to dominate above 2.5μm meaning that it is not beneficial to extend to such wavelengths. For LIDAR applications, a large signal-to-noise ratio (SNR) is desirable for depth resolution [28]. As integration time is proportional to SNR^2 the reduction of background counts results in a quadratic reduction in the integration time required for a given SNR. Utilizing single-photon detectors offers unique advantages for free-space applications such as imaging or communication [29] as the range for a fixed optical power source is maximized. In addition to this, operating in the mid-infrared with low output powers allows eye-safe and covert operation.

3. Device design

As stated in section 1, SNSPDs have demonstrated spectral sensitivity far into the mid-infrared. That said, it remains an engineering challenge to optimize the device design parameters to fabricate devices with high system detection efficiency (SDE) as has been achieved for the best 1.55μm devices. Off the shelf in-fiber optical components are not generally available commercially and standard silica fiber has a cut off wavelength at 2.3μm. Devices coupled to silica fiber with system detection efficiencies of 20% at 2μm have been reported [30] and others have been successfully coupled with chalcogenide infrared fiber [31]. For this work the devices were based on a 6nm NbTiN film (T_c of 7K) patterned into a 60nm wide nanowire with an 80nm gap meandering over a 15μm by 15μm active-area. This nanowire was embedded in an optical cavity designed to enhance absorption in the mid-infrared and the device is then capped with an Ag mirror on top. Figure 2(b) shows a schematic of the device design. 2.3μm was chosen as the operational wavelength as it is the cut off for easily available and robust SM2000 single-mode silica fiber [32] as well as sitting in the agreeable transmission window shown in Fig. 1. In order to deliver photons onto the nanowire an SM2000 fiber with ceramic ferrule is first glued into a copper fiber holding piece. The device is then mounted into a sample mount and and the tip of the fiber is aligned with the the active-area through the back of the substrate using an InGaAs camera and 1.55μm laser to ensure photons are delivered to the active-area. The backside coupling approach does lead to losses due to the broadening of the beam radius as it travels through the substrate - these are discussed in section 5.

The device was characterized at 2.3μm by utilizing an optical parametric oscillator (Spark OPO from Chromacity Ltd) to generate short pulses (~ps) at 110MHz. As the output of the OPO was spectrally broad we coupled it into a free-space filtering setup through a narrow bandpass filter (Spectrogon, CW 2328+/-43nm) and then re-coupled it back into single-mode fiber to give us a narrow linewidth fast source. The OPO is tuneable from 1.5 to 4.2μm and all of the free-space components have been chosen for their wide spectral range allowing the overall source to be tuneable in this range by substituting the bandpass filter for one at the desired wavelength. For characterization of the detectors we then attenuated this output down to single-photon level by constructing another free-space filtering setup similar to the first but utilizing neutral density (ND) filters for attenuation. With the output power of the OPO (tens of mWs), the flat response of our ND filters across the infrared spectrum and a standard off the shelf power meter (Thorlabs S148C) we could calibrate up to 45dB of fixed attenuation. For efficiency measurements we attenuated the output of the OPO down to 0.5 photons per pulse using this setup. With the 30% coupling efficiency and 50% absorption efficiency estimated in section 5 this gives us 0.075

Optics EXPRESS

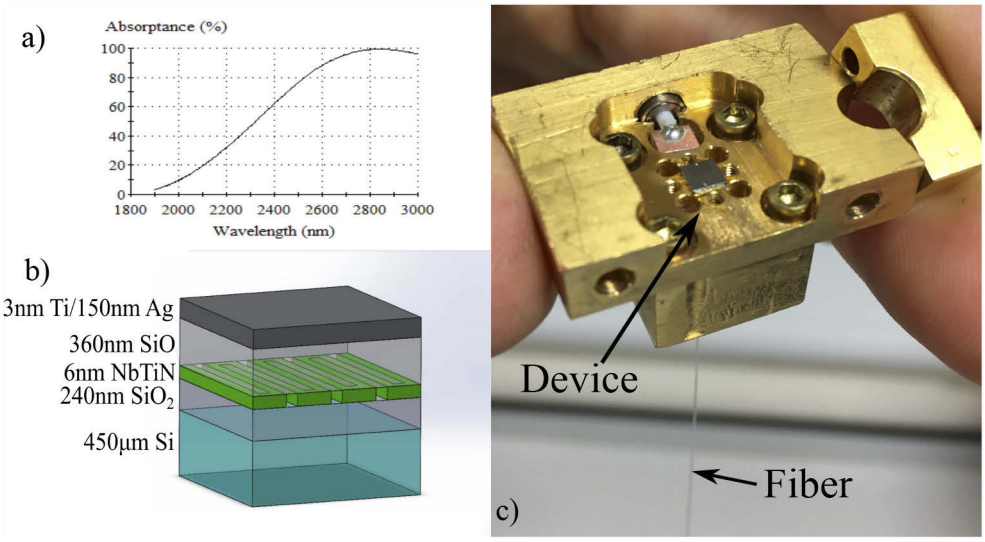

Fig. 2. a): Simulation of the absorption in the SNSPD cavity design. b): Schematic of the device design showing the nanowire (green) embedded in the optical stack. The device is optically fiber-coupled from the underside of the device (bottom of figure). c): Photo showing the mounted device and the fiber aligned through the underside of the device.

absorbed photons per pulse. Following Poisson statistics, the probability of a detector click being caused by multiple photons being absorbed is therefore <0.3% so it is reasonable to conclude that the detector is single-photon sensitive. The SDE was then computed by subtracting the dark count rate from the photon count rate and dividing by the input photon flux. It should be noted here that the reference point for the SDE was an FC/PC connector on the outside of the cryostat therefore the SDE figures calculated will include bend-induced fiber losses, splice losses (of which there are two in the cryostat) and the loss of the FC/PC connector that the photons are input to. The photon count rate (PCR) and dark count rate (DCR) are shown in Fig. 3(a). It is interesting to note in Fig. 3(a) the DCR does not follow the expected curve for the best devices at 1.55μm, exhibiting a slow onset of dark counts in the 6 to 8μA range before the expected exponential increase as the current approaches I_c. This has been observed in similar devices designed for longer wavelengths [31] and is due to blackbody photons being coupled into the IR fiber from optical components at room temperature. Cold optical filtering [33] will be useful in suppression of this blackbody radiation in future work. For these characterization results, polarization was controlled using a manual polarization controller to maximize the count rate of the SNSPD. Once the SDE against bias data was taken we selected an optimum bias point of 7.5μA, giving us a reasonable dark count rate of 1000 counts per second and just over 1% SDE. This point was used for the rest of the experiments including the IRF data and the LIDAR experiment. The maximum count rate of the device was estimated from the recovery time of the detector (100ns) to be 10MHz.

The instrument response function (IRF) used to determine the system timing jitter and also to calculate the peak position in the LIDAR returns was measured using the filtered OPO source described above. The sync output of the OPO was fed into a fast photodetector (Thorlabs DET08CFC) to give a sync pulse for the HydraHarp time correlated single-photon counting (TCSPC) module. The idler output was sent through the LIDAR setup described in section 4 and reflected from a metallic flat surface. A histogram was built up and the timing jitter FWHM was calculated by fitting a Gaussian distribution to the data. This is presented in Fig. 4(b). There is

Optics EXPRESS

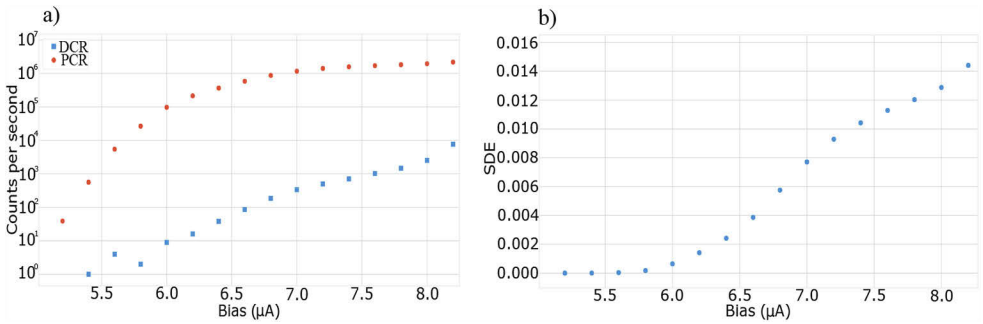

Fig. 3. a) Photon count rate (red) and dark count rate (blue) for 2.3μm wavelength photons incident on the device at 2.5K. The early onset of the DCR before the exponential increase as the current approaches the critical current is caused by black body radiation coupling into the fiber from room temperature. b) Calculated system detection efficiency (SDE) against bias current. For these devices at an operating temperature of 2.5K we do not observe the characteristic plateau associated with saturation of the internal detection efficiency. The relatively low overall SDE observed is discussed in section 5.

noticeable asymmetry in the data with the IRF exhibiting an exponential tail. This is in line with other observed results [34–36] though the origin of the tail is still unclear.

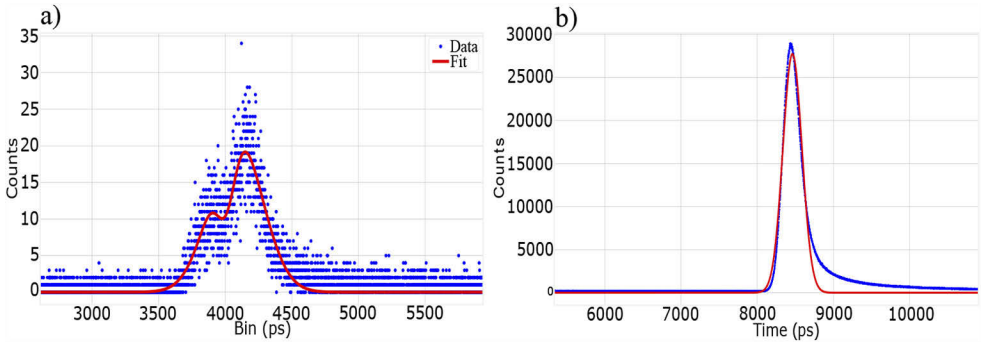

Fig. 4. a): Results from two cardboard squares separated by 40mm and co-illuminated with a 2mm beam. The data is fitted with a double Gaussian function to determine the peak positions. The integration time was 10s for this measurement. Below 4cm separation the two peaks become difficult to distinguish. b): Instrument response function of the entire LIDAR setup described in section 4 showing a system timing jitter of 280ps FWHM fitted with a Gaussian function. Blue dots show data points and the red line is the fit.

4. Single-photon LIDAR

These devices were cooled to 2.5K in a closed-cycle Gifford-McMahon type cryostat and deployed into a basic tabletop LIDAR setup, a schematic of which is shown in Fig. 5. The OPO provided 2.3μm photons by passing the output through the bandpass filtering setup outlined in section 3 and the output power was adjusted either using neutral density filters in the filtering setup or by misalignment of the output coupler. An initial test was performed where two non-reflective surfaces (white cardboard sheets) were illuminated by the outgoing beam and the returns collected. A simple double Gaussian was fitted to the data to determine the separation of the targets. The separation was slowly decreased until the two surfaces could no longer be distinguished by the

Optics EXPRESS

fitting - thus giving us a measure of the depth resolution of the system. Figure 4(a) shows a separation of 40mm being measured by this method. If we take the peak positions from the Gaussian fitting at 3910ps and 4153ps respectively we can see that the separation of the two targets is 37mm, well aligned with the manual measurement of 40mm. Next we placed two motorized translation stages mounted in an XY configuration at a distance of 350mm from the beam output. By placing the target on a stage attached to this setup we could scan the target through the beam to give a 50x50mm image. A LEGO model of Big Ben was chosen as it gave an easily recognizable feature with a variety of shaped edges and corners. Figure 6(b) shows a depth image of the model. Although the scan area was smaller than the total model, key features can easily be picked out including the raised clock face, edges of the tower and holes below the spire. This image was taken with an average emitted power of <12μW and an integration time of 1s per pixel. For this test each pixel was computed by simple cross correlation of the instrument response function (IRF) shown in Fig. 4(b) to give the peak position. In the image presented here the cardboard background was scaled to provide finer detail in the image. All of the above data was taken in a brightly lit lab.

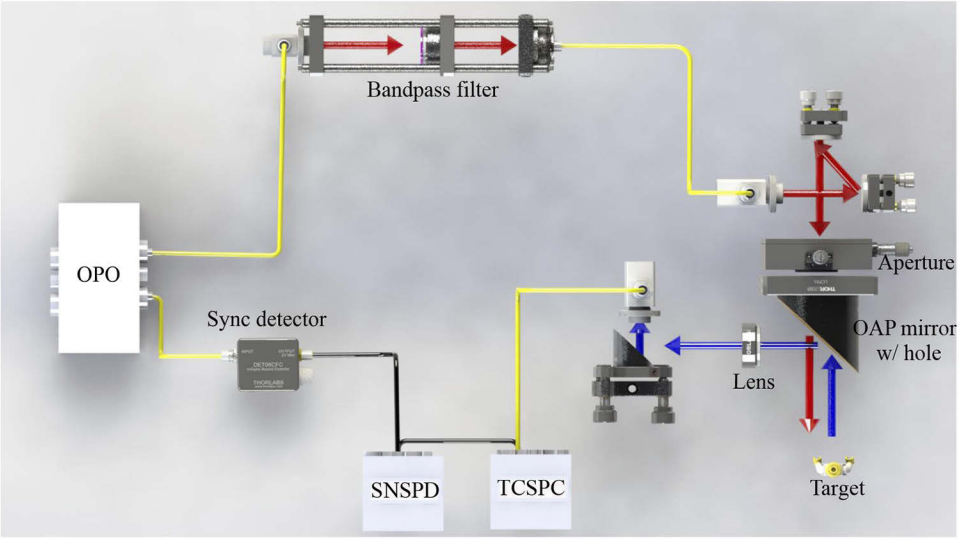

Fig. 5. LIDAR schematic. The OPO provides a sync pulse which is fed into a fast photodetector (Thorlabs DET08CFC) to provide the sync signal (START) for the HydraHarp TCSPC module. The idler pulse travels through the free-space filtering system described in the text (seen at the top of the figure) and is then directed through the central hole of an off-axis parabolic (OAP) mirror with a 3.2mm through hole to the target. An aperture before this hole controls the beam size. Once reflected from the target (LEGO figure) returns are collected and focussed into fiber with two OAP mirrors and a plano-convex lens and then delivered to the SNSPD. Electrical response signals from the SNSPD are then amplified and sent to the TCSPC to provide the STOP signal. SM2000 fiber is shown in yellow, electrical connections in black. Arrows indicate free-space transmission with red being output and blue the target returns.

Optics EXPRESS

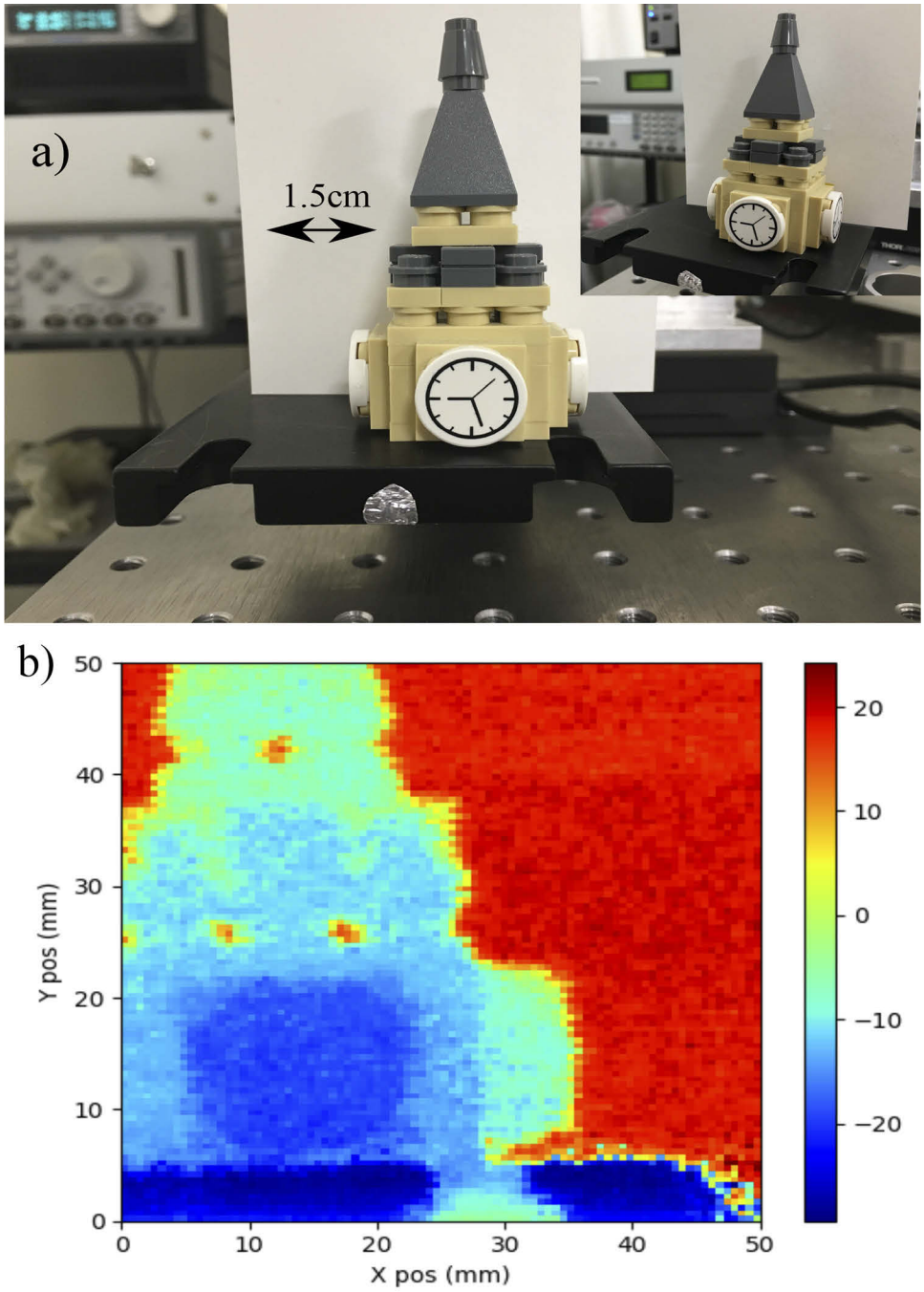

Fig. 6. a) Photos of LEGO Big Ben model on motorized stages scanning in X and Y. The main photo shows the target as viewed by the LIDAR apparatus and the inset shows the depth profile from the side. b) LIDAR depth image acquired with a 1s integration time per pixel. The whole area of the model has not been scanned. Key features such as the raised clock face (3mm depth from next surface), holes in the model and curved cutout of the moving stage can be easily picked out. The scale bar shows depth in mm.

Optics EXPRESS

5. Discussion

As is shown in section 4 reasonable depth images can be obtained using a simple and fast cross correlation of the IRF with the returns histogram. As has been demonstrated in other work, deploying more advanced algorithms such as a reversible jump Markov chain Monte Carlo (RJMCMC) or Maximum Likelihood Estimates(MLE) [37,38] would result in enhanced multi peak detection in few-photon returns but the implementation of such an algorithm is out with the scope of this work.

The cavity design presented here has been simulated using the Essential Macleod software package to have a peak optical absorption at around 2.8μm (simulated at 100% absorptance), somewhat higher than the operating wavelength of 2.3μm (simulated at 50%). For these simulations the n and k values were measured for a NbTiN thin film using variable angle spectroscopic ellipsometry (VASE), see [39]. This low absorption efficiency is a contribution to the low SDE observed for these devices. Another issue with working at 2.3μm is that the bending losses of SM2000 fiber at this wavelength are, although better than for standard telecom fiber, still significant (>5dB for <10mm bend radius). Although care was taken to avoid bends in the fiber outside the cryostat, the bare fiber coupling the detector at 2.5K to the outside at 300K had some unavoidable bends due to the small area available inside. In a separate test 1m of bare fiber was placed into a cryostat configuration and the loss measured was 0.7dB at 2.3μm. Taking into account the length of fiber used inside the cryostat for the LIDAR experiments (2m) and some non-negligible splicing loss it is not unreasonable that the fiber loss approaches 2dB.

Lastly, as the fiber is aligned with the backside of the device and the nanowire is illuminated through the substrate, there is a 450μm gap between the fiber end face and the nanowire. Following calculations outlined in [40] using values for SM2000 fiber at 2.3μm we find that the beam radius is ~51μm after the 450μm of substrate. Given the active-area of the device is 15μm by 15μm then only ~30% of the beam will be incident on the active-area. A solution shown in [41] for similar devices was to implement a gradient index (GRIN) lens on the fiber endface to focus the output onto the active-area. This approach could be implemented here though commercial on-fiber GRIN lenses for the mid-infrared are not readily available. Other solutions could include a larger active-area device to negate the effect of the beam broadening but this would come with the cost of lower maximum count rate as the size increases. Recent work on large area detectors to improve the count rate shows promise [42]. A simpler approach could be to switch to frontside coupled detectors [43] as then gap between the fiber end face and the nanowire would be negligible. This approach works well for other research groups and is the focus of future work as we can minimize coupling losses while retaining the ease and deployability of fiber-coupled detectors.

The above absorption efficiency, coupling efficiency and fiber losses all add up to give an estimated efficiency of 9%, still higher than our experimentally measured value of <2%. If we examine the efficiency vs bias curve shown in Fig. 3(b) we see that the efficiency does not saturate or exhibit a plateau as bias current increases. This indicates that we have not achieved saturated internal detection efficiency within the nanowire for this wavelength and this is where the disparity between the measured and estimated efficiency values arises. Possible solutions to this could be to optimize nanowire geometry, film growth and material selection as discussed below. Other post fabrication techniques such as ion implantation designed to suppress the superconducting energy gap and enhance the internal efficiency have also recently been demonstrated [44].

The low SDE observed will be addressed in future work which will concentrate on frontside coupling these devices with mid-infrared chalcogenide or fluoride based fibers to enable access to the higher absorption area while minimizing the bend losses. The wavelength range closer to 3μm covers the absorption lines of many greenhouse and industrial gases that hold interest for environmental monitoring purposes. Characterization of our detectors in this regime would hold

Optics EXPRESS

enormous potential for future remote sensing applications such as differential absorption LIDAR (DIAL) for gas monitoring [45].

The low critical currents (I_c=8 to 9μA) observed for these devices contribute to the relatively high timing jitter observed. The low I_c results in low pulse height and poor signal-to-noise which has been shown to give a higher jitter device [46]. This could be attributed to fabrication imperfections in the narrow nanowires causing constrictions in the wire and square bends used on the ends of the meander - there is significant evidence to show that rounded meander bends minimize current constriction effects in the corners [47]. The uniformity of the superconducting film over the active-area could also contribute to this effect.

With the discussion of the deficiencies of the detectors addressed above we shall now consider what design parameters we will look to optimize for future fabrication of mid-infrared SNSPDs. SDE is the current focus for future detectors as, as shown in section 3, detectors with SDE over around 20% have not yet been demonstrated and SDE figures for wavelengths above 2.3μm are scarce. Minimization of the cross-section of the nanowires is a key controllable fabrication parameter to increase SDE as photon energy lowers at longer wavelengths - the probability of a smaller hotspot turning the entire nanowire resistive will scale with cross section. However, as discussed above, this will result in a smaller I_c - even if fabrication is perfect - leading to a higher timing jitter and worse SNR. This can be somewhat mitigated by the use of low noise cryogenic amplification as shown by other groups [14] and these amplifiers will be implemented in future work. In tandem with minimization of cross section, material selection will play a crucial role. The amorphous materials WSi and MoSi have been the usual choice for longer wavelength devices as the smaller superconducting energy gap (MoSi=2.28meV, WSi=1.52meV when compared to NbN=4.9meV. Values are for bulk [48]) leads to a higher probability of triggering for lower energy photons, although this comes with a lower critical temperature meaning that high effiency WSi or MoSi devices at 2.5K are unlikely. With carefully selected high quality films, fabrication of small cross-section nanowires and coupling with specialist mid-infrared fibers development of SNSPDs for mid-infrared will result in fast, high efficiency detectors for a large range of wavelengths currently not covered by semiconductor single-photon detectors alternatives.

6. Conclusion

We have presented a first proof-of-principle single-photon LIDAR system at 2.3μm wavelength using SNSPDs. We have demonstrated the potential of SNSPDs for few-photon mid-infrared free-space applications such as the imaging work presented here. We have also constructed and utilized a tuneable characterization setup for 1.5 to 4.2μm wavelength photons which will be scalable as we move to detectors optimized for longer wavelengths. In future work we will look to enhance the SDE and timing jitter in the mid-infrared by fabrication of ultra-narrow (sub 50nm width) constriction-free nanowires embedded in optical cavities and coupled with specialist infrared optical fiber. We will also incorporate cryogenic amplifiers in a differential readout scheme [49] to remove the geometric component of the timing jitter from the large nanowire meanders. These improved devices can be installed in the current LIDAR setup to give improved depth resolution at smaller pixel integration times and also deployed in outdoor field trials to demonstrate their improved operation in broad daylight when compared to shorter wavelength systems.

Funding

European Research Council (IRIS 648604); Engineering and Physical Sciences Research Council (EP/M01326X/1); Japan Science and Technology Agency (JPMXS0118067634).

Optics EXPRESS

Acknowledgments

R.H.H. acknowledges a Royal Society Leverhulme trust senior research fellowship. K.E. gratefully acknowledges an internship at NICT Japan.

Disclosures

The authors declare no conflicts of interest.

References

1. M.-C. Amann, T. M. Bosch, M. Lescure, R. A. Myllylae, and M. Rioux, "Laser ranging: a critical review of unusual techniques for distance measurement," Opt. Eng. **40**(1), 10–20 (2001).
2. G. S. Buller and A. Wallace, "Ranging and three-dimensional imaging using time-correlated single-photon counting and point-by-point acquisition," IEEE J. Sel. Top. Quantum Electron. **13**(4), 1006–1015 (2007).
3. V. Kovaltchouk, G. Lolos, Z. Papandreou, and K. Wolbaum, "Comparison of a silicon photomultiplier to a traditional vacuum photomultiplier," Nucl. Instrum. Methods Phys. Res., Sect. A **538**(1-3), 408–415 (2005).
4. M. Ghioni, A. Gulinatti, I. Rech, F. Zappa, and S. Cova, "Progress in silicon single-photon avalanche diodes," IEEE J. Sel. Top. Quantum Electron. **13**(4), 852–862 (2007).
5. A. Y. Loudon, P. A. Hiskett, G. S. Buller, R. T. Carline, D. C. Herbert, W. Leong, and J. G. Rarity, "Enhancement of the infrared detection efficiency of silicon photon-counting avalanche photodiodes by use of silicon germanium absorbing layers," Opt. Lett. **27**(4), 219–221 (2002).
6. F. Zappa, A. Tosi, and S. Cova, "InGaAs SPAD and electronics for low time jitter and low noise," in *Photon Counting Applications, Quantum Optics, and Quantum Cryptography*, vol. 6583 (International Society for Optics and Photonics, 2007), p. 65830E.
7. M. D. Eisaman, J. Fan, A. Migdall, and S. V. Polyakov, "Invited review article: Single-photon sources and detectors," Rev. Sci. Instrum. **82**(7), 071101 (2011).
8. B. Matveev, M. Aidaraliev, G. Gavrilov, N. Zotova, S. Karandashov, G. Sotnikova, N. Stus, G. Talalakin, N. Il'inskaya, and S. Aleksandrov, "Room temperature InAs photodiode–InGaAs led pairs for methane detection in the mid-IR," Sens. Actuators, B **51**(1-3), 233–237 (1998).
9. M. B. Reine, "HgCdTe photodiodes for IR detection: A review," in *Photodetectors: Materials and Devices VI*, vol. 4288 (International Society for Optics and Photonics, 2001), pp. 266–278.
10. J. S. Dam, P. Tidemand-Lichtenberg, and C. Pedersen, "Room-temperature mid-infrared single-photon spectral imaging," Nat. Photonics **6**(11), 788–793 (2012).
11. G. Gol'tsman, O. Okunev, G. Chulkova, A. Lipatov, A. Semenov, K. Smirnov, B. Voronov, A. Dzardanov, C. Williams, and R. Sobolewski, "Picosecond superconducting single-photon optical detector," Appl. Phys. Lett. **79**(6), 705–707 (2001).
12. F. Marsili, V. B. Verma, J. A. Stern, S. Harrington, A. E. Lita, T. Gerrits, I. Vayshenker, B. Baek, M. D. Shaw, R. P. Mirin, and S. W. Nam, "Detecting single infrared photons with 93% system efficiency," Nat. Photonics **7**(3), 210–214 (2013).
13. H. Shibata, K. Shimizu, H. Takesue, and Y. Tokura, "Ultimate low system dark-count rate for superconducting nanowire single-photon detector," Opt. Lett. **40**(14), 3428–3431 (2015).
14. B. Korzh, Q. Zhao, S. Frasca, J. Allmaras, T. Autry, E. Bersin, M. Colangelo, G. Crouch, A. Dane, T. Gerrits, F. Marsili, G. Moody, E. Ramirez, J. Rezac, M. Stevens, E. Wollman, D. Zhu, P. Hale, K. Silverman, R. Mirin, S. Nam, M. Shaw, and K. Berggren, "Demonstrating sub-3 ps temporal resolution in a superconducting nanowire single-photon detector," arXiv preprint arXiv:1804.06839 (2018).
15. F. Marsili, F. Bellei, F. Najafi, A. E. Dane, E. A. Dauler, R. J. Molnar, and K. K. Berggren, "Efficient single photon detection from 500 nm to 5 μm wavelength," Nano Lett. **12**(9), 4799–4804 (2012).
16. V. Verma, A. Lita, B. Korzh, E. Wollman, M. Shaw, R. Mirin, and S. Nam, "Towards single-photon spectroscopy in the mid-infrared using superconducting nanowire single-photon detectors," in *Advanced Photon Counting Techniques XIII*, vol. 10978 (International Society for Optics and Photonics, 2019), p. 109780N.
17. L. Chen, D. Schwarzer, J. A. Lau, V. B. Verma, M. J. Stevens, F. Marsili, R. P. Mirin, S. W. Nam, and A. M. Wodtke, "Ultra-sensitive mid-infrared emission spectrometer with sub-ns temporal resolution," Opt. Express **26**(12), 14859–14868 (2018).
18. R. H. Hadfield, "Single-photon detectors for optical quantum information applications," Nat. Photonics **3**(12), 696–705 (2009).
19. C. M. Natarajan, M. G. Tanner, and R. H. Hadfield, "Superconducting nanowire single-photon detectors: physics and applications," Supercond. Sci. Technol. **25**(6), 063001 (2012).
20. M. J. Stevens, R. H. Hadfield, R. E. Schwall, S. W. Nam, R. P. Mirin, and J. A. Gupta, "Fast lifetime measurements of infrared emitters using a low-jitter superconducting single-photon detector," Appl. Phys. Lett. **89**(3), 031109 (2006).
21. M. Shaw, F. Marsili, A. Beyer, J. Stern, G. Resta, P. Ravindran, S. Chang, J. Bardin, D. Russell, J. Gin, F. Patawaran, V. Verma, R. Mirin, S. Nam, and W. Farr, "Arrays of WSi superconducting nanowire single photon detectors for

Optics EXPRESS

deep-space optical communications," in *2015 Conference on Lasers and Electro-Optics (CLEO)*, (IEEE, 2015), pp, 1–2.
22. A. McCarthy, N. J. Krichel, N. R. Gemmell, X. Ren, M. G. Tanner, S. N. Dorenbos, V. Zwiller, R. H. Hadfield, and G. S. Buller, "Kilometer-range, high resolution depth imaging via 1560 nm wavelength single-photon detection," Opt. Express **21**(7), 8904–8915 (2013).
23. H. Zhou, Y. He, L. You, S. Chen, W. Zhang, J. Wu, Z. Wang, and X. Xie, "Few-photon imaging at 1550 nm using a low-timing-jitter superconducting nanowire single-photon detector," Opt. Express **23**(11), 14603–14611 (2015).
24. J. Zhu, Y. Chen, L. Zhang, X. Jia, Z. Feng, G. Wu, X. Yan, J. Zhai, Y. Wu, Q. Chen, X. Zhou, Z. Wang, C. Zhang, L. Kang, J. Chen, and P. Wu, "Demonstration of measuring sea fog with an SNSPD-based lidar system," Sci. Rep. **7**(1), 15113 (2017).
25. D. Salvoni, M. Ejrnaes, L. Parlato, A. Sannino, A. Boselli, G. Pepe, R. Cristiano, and X. Wang, "Lidar techniques for a SNSPD-based measurement," in *Journal of Physics: Conference Series*, vol. 1182 (IOP Publishing, 2019), p. 012014.
26. American Society for Testing and Materials. Committee G03 on Weathering and Durability, *Standard tables for reference solar spectral irradiances: direct normal and hemispherical on 37° tilted surface* (ASTM international, 2003).
27. R. V. Kochanov, I. Gordon, L. Rothman, P. Wcisło, C. Hill, and J. Wilzewski, "Hitran application programming interface (hapi): A comprehensive approach to working with spectroscopic data," J. Quant. Spectrosc. Radiat. Transfer **177**, 15–30 (2016).
28. S. Pellegrini, G. S. Buller, J. M. Smith, A. M. Wallace, and S. Cova, "Laser-based distance measurement using picosecond resolution time-correlated single-photon counting," Meas. Sci. Technol. **11**(6), 712–716 (2000).
29. S. Prabhakar, T. Shields, A. Dada, M. Ebrahim, G. G. Taylor, D. Morozov, K. Erotokritou, S. Miki, M. Yabuno, H. Terai, C. Gawith, M. Kues, L. Caspani, R. H. Hadfield, and M. Clerici, "Two-photon quantum interference and entanglement at 2 μm," arXiv preprint arXiv:1906.02082 (2019).
30. A. Divochiy, M. Misiaszek, Y. Vakhtomin, P. Morozov, K. Smirnov, P. Zolotov, and P. Kolenderski, "Single photon detection system for visible and infrared spectrum range," Opt. Lett. **43**(24), 6085–6088 (2018).
31. F. Marsili, V. Verma, M. Stevens, J. Stern, M. Shaw, A. Miller, D. Schwarzer, A. Wodtke, R. Mirin, and S. Nam, "Mid-infrared single-photon detection with tungsten silicide superconducting nanowires," in *CLEO: Science and Innovations*, (Optical Society of America, 2013), pp. CTu1H–1.
32. P. S. Kuo, "Using silica fiber coupling to extend superconducting nanowire single-photon detectors into the infrared," OSA Continuum **1**(4), 1260–1266 (2018).
33. H. Shibata, K. Shimizu, H. Takesue, and Y. Tokura, "Superconducting nanowire single-photon detector with ultralow dark count rate using cold optical filters," Appl. Phys. Express **6**(7), 072801 (2013).
34. F. Najafi, "Timing performance of superconducting nanowire single-photon detectors," Ph.D. thesis, Massachusetts Institute of Technology, (2015).
35. M. Sidorova, A. Semenov, H.-W. Húbers, I. Charaev, A. Kuzmin, S. Doerner, and M. Siegel, "Physical mechanisms of timing jitter in photon detection by current-carrying superconducting nanowires," Phys. Rev. B **96**(18), 184504 (2017).
36. R. H. Hadfield and G. Johansson, *Superconducting devices in quantum optics* (Springer, 2016).
37. S. Hernandez-Marin, A. M. Wallace, and G. J. Gibson, "Multilayered 3d lidar image construction using spatial models in a bayesian framework," IEEE Trans. Pattern Anal. Mach. Intell. **30**(6), 1028–1040 (2008).
38. S. Hernandez-Marin, A. M. Wallace, and G. J. Gibson, "Bayesian analysis of lidar signals with multiple returns," IEEE Trans. Pattern Anal. Mach. Intell. **29**(12), 2170–2180 (2007).
39. A. Banerjee, R. M. Heath, D. Morozov, D. Hemakumara, U. Nasti, I. Thayne, and R. H. Hadfield, "Optical properties of refractory metal based thin films," Opt. Mater. Express **8**(8), 2072–2088 (2018).
40. A. M. Kowalevicz Jr and F. Bucholtz, "Beam divergence from an smf-28 optical fiber," Tech. rep., Naval Research Lab, Washington DC, (2006).
41. S. Miki, T. Yamashita, H. Terai, and Z. Wang, "High performance fiber-coupled NbTiN superconducting nanowire single photon detectors with Gifford-McMahon cryocooler," Opt. Express **21**(8), 10208–10214 (2013).
42. C. Zhang, W. Zhang, J. Huang, L. You, H. Li, C. lv, T. Sugihara, M. Watanabe, H. Zhou, Z. Wang, and X. Xie, "NbN superconducting nanowire single-photon detector with an active area of 300 μm-in-diameter," AIP Adv. **9**(7), 075214 (2019).
43. V. Verma, F. Marsili, B. Baek, A. Lita, T. Gerrits, J. Stern, R. Mirin, and S. W. Nam, "55% system detection efficiency with self-aligned WSi superconducting nanowire single-photon detectors," in *2012 Conference on Lasers and Electro-Optics (CLEO)*, (IEEE, 2012), pp. 1–2.
44. W. Zhang, Q. Jia, L. You, X. Ou, H. Huang, L. Zhang, H. Li, Z. Wang, and X. Xie, "Saturating intrinsic detection efficiency of superconducting nanowire single-photon detectors via defect engineering," Phys. Rev. Appl. **12**(4), 044040 (2019).
45. O. Romanovskii, "Airborne DIAL lidar gas analysis of the atmosphere by middle IR gas lasers: Numerical modeling," Opt. Mem. Neural Networks **17**(2), 131–137 (2008).
46. L. You, X. Yang, Y. He, W. Zhang, D. Liu, W. Zhang, L. Zhang, L. Zhang, X. Liu, S. Chen, Z. Wang, and X. Xie, "Jitter analysis of a superconducting nanowire single photon detector," AIP Adv. **3**(7), 072135 (2013).

Optics EXPRESS

47. J. R. Clem and K. K. Berggren, "Geometry-dependent critical currents in superconducting nanocircuits," Phys. Rev. B **84**(17), 174510 (2011).
48. A. E. Lita, V. B. Verma, R. D. Horansky, J. M. Shainline, R. P. Mirin, and S. Nam, "Materials development for high efficiency superconducting nanowire single-photon detectors," MRS Online Proc. Libr. Arch. **1807**, 1–6 (2015).
49. N. Calandri, Q.-Y. Zhao, D. Zhu, A. Dane, and K. K. Berggren, "Superconducting nanowire detector jitter limited by detector geometry," Appl. Phys. Lett. **109**(15), 152601 (2016).